The Astrophysical Journal, 594:651–663, 2003 September 1

LINE INTENSITIES AND MOLECULAR OPACITIES OF THE FeH $F\ ^4\Delta_i$–$X\ ^4\Delta_i$ TRANSITION

M. Dulick,[1] C. W. Bauschlicher, Jr.,[2] Adam Burrows,[3] C. M. Sharp,[3]
R. S. Ram,[4] and Peter Bernath[4,5]

Received 2003 January 2; accepted 2003 May 2

ABSTRACT

We calculate new line lists and opacities for the $F\ ^4\Delta_i$–$X\ ^4\Delta_i$ transition of FeH. The 0–0 band of this transition is responsible for the Wing-Ford band seen in M-type stars, sunspots, and brown dwarfs. The new Einstein A-values for each line are based on a high-level ab initio calculation of the electronic transition dipole moment. The necessary rotational line strength factors (Hönl-London factors) are derived for both the Hund's case (a) and (b) coupling limits. A new set of spectroscopic constants was derived from the existing FeH term values for $v = 0$, 1, and 2 levels of the X and F states. Using these constants, extrapolated term values were generated for $v = 3$ and 4 and for J-values up to 50.5. The line lists (including Einstein A-values) for the 25 vibrational bands with $v \leq 4$ were generated using a merged list of experimental and extrapolated term values. The FeH line lists were used to compute the molecular opacities for a range of temperatures and pressures encountered in L and M dwarf atmospheres. Good agreement was found between the computed and observed spectral energy distribution of the L5 dwarf 2MASS-1507.

Subject headings: infrared: stars — line: identification — molecular data — stars: atmospheres — stars: fundamental parameters — stars: low-mass, brown dwarfs

On-line material: machine-readable table

1. INTRODUCTION

Wing & Ford (1969) were the first to detect a mysterious band near 9910 Å in late M dwarfs on the basis of low-resolution spectra. The Wing-Ford band was later found in S stars (Wing 1972) and in sunspots at higher spectral resolution by Wing, Cohen, & Brault (1977). Nordh, Lindgren, & Wing (1977) identified the Wing-Ford band as the 0–0 band of an FeH electronic transition by comparison with an unassigned laboratory spectrum of FeH that showed a head at 9896 Å degraded to longer wavelengths. Laboratory spectra of the 1–0 band of this FeH transition show a head at 8691 Å (Carroll, McCormack, & O'Connor 1976), and this band is also seen in sunspots (Wing et al. 1977). Fawzy, Youssef, & Engvold (1998) have detected the 2–0 and 2–1 bands in sunspots.

FeH bands can be observed well past 1 μm with the 0–1 band of the $F\ ^4\Delta_i$–$X\ ^4\Delta_i$ transition easily visible near 1.19 μm in sunspots (Wallace & Hinkle 2001b). A new electronic transition of FeH has been identified near 1.583 μm in late M dwarfs, early L dwarfs (Leggett et al. 2001; Cushing et al. 2003), and sunspots (Wallace & Hinkle 2001a). Although not assigned yet, the 1.583 μm band is probably the $E\ ^4\Pi$–$A\ ^4\Pi$ transition of FeH on the basis of a comparison with a laboratory spectrum and the ab initio calculation of Langhoff & Bauschlicher (1990). Wilson & Brown (2001) have tentatively identified two spin components of the $A\ ^4\Pi$ state about 1000 cm^{-1} above the $X\ ^4\Delta_{7/2}$ spin component by low-resolution dispersed laser-induced fluorescence.

On the astronomical front, there have also been recent advances in FeH observations. The Wing-Ford band has been found in a wide variety of sources, including galaxies (e.g., Hardy & Couture 1988). The most important application of the $F\ ^4\Delta_i$–$X\ ^4\Delta_i$ transition is, however, in the spectroscopy of L-type brown dwarfs. Indeed, the presence of the metal hydrides (FeH and CrH) and the absence of the metal oxides (TiO and VO) are the defining characteristics of L-type brown dwarfs (Kirkpatrick et al. 1999a, 1999b, 2000). The main source of opacity near 1 μm is the $A\ ^6\Sigma^+$–$X\ ^6\Sigma^+$ transition of CrH and the $F\ ^4\Delta_i$–$X\ ^4\Delta_i$ transition of FeH.

Missing in all of the work on FeH is a measurement of the oscillator strength of any of the FeH transitions. Without line strengths, it is not possible to determine the column densities of FeH from observations, and the physical properties of the atmospheres also depend on the FeH opacity. Schiavon, Barbuy, & Singh (1997) have provided some line strengths for the $F\ ^4\Delta_i$–$X\ ^4\Delta_i$ transition by arbitrarily choosing an oscillator strength of 10^{-3}, at variance with the value calculated by Langhoff & Bauschlicher (1990). In addition, they seem to have made some computational errors, perhaps associated with the degeneracy factors. We decided, therefore, to apply to FeH the methods we used in our recent calculation of the line strengths and opacity of the $A\ ^6\Sigma^+$–$X\ ^6\Sigma^+$ transition of CrH (Bauschlicher et al. 2001; Burrows et al. 2002). We thus carried out a new ab initio calculation of the transition dipole moment of the $F\ ^4\Delta_i$–$X\ ^4\Delta_i$ transition of FeH. In addition, we have derived analytical expressions for the Hönl-London rotational line strength factors for $^4\Delta$–$^4\Delta$ transitions in both the Hund's case (a) and Hund's case (b) limits. The existing term values of Phillips et al. (1987) were extrapolated to higher J and v based on a new determination of the spectroscopic constants.

In the laboratory, early work in Ireland (McCormack & O'Connor 1976) and Sweden (Klynning & Lindgren 1973)

[1] National Solar Observatory, 950 North Cherry Avenue, P.O. Box 26732, Tucson, AZ 85726-6732.
[2] NASA Ames Research Center, Mailstop 230-3, Moffett Field, CA 94035; charles.w.bauschlicher@nasa.gov.
[3] Department of Astronomy and Steward Observatory, University of Arizona, 933 North Cherry Avenue, Tucson, AZ 85721; burrows@jupiter.as.arizona.edu, csharp@as.arizona.edu.
[4] Department of Chemistry, University of Arizona, Tucson, AZ 85721; rram@u.arizona.edu.
[5] Department of Chemistry, University of Waterloo, Waterloo, ON N2L 3G1, Canada; bernath@uwaterloo.ca.

provided line lists but no rotational assignments. The Wing-Ford band was established as a $^4\Delta$–$^4\Delta$ transition by rotational analysis of the 1–0 and 0–0 bands of FeD by Balfour, Lindgren, & O'Connor (1983). The more heavily perturbed FeH bands finally yielded to rotational analysis by Phillips et al. (1987), who assigned the 2–0 (7786 Å), 1–0 (8692 Å), 2–1 (9020 Å), 0–0 (9896 Å), 1–1 (10253 Å), 0–1 (11939 Å), and 1–2 bands (12389 Å). These bands were recorded by Fourier transform emission spectroscopy using a carbon tube furnace at 2200°C–2450°C with 75–500 torr of H_2 and He. The Phillips et al. (1987) paper is still the definitive work on the 1 μm bands of FeH.

It was not clear in the early work that the lower state of the Wing-Ford band was, in fact, the ground state of FeH. Both ab initio calculations (Walch 1984) and photoelectron spectroscopy of FeH^- (Stevens, Feigerle, & Lineberger 1983) provided strong evidence for an $X\ ^4\Delta$ ground state. Langhoff & Bauschlicher (1990) located all of the low-lying electronic states by ab initio calculation and suggested the label $F\ ^4\Delta_i$–$X\ ^4\Delta_i$ for the 1 μm band system. (The right subscript i stands for inverted and indicates the four spin components with $\Omega = 7/2, 5/2, 3/2, \frac{1}{2}$ increase in energy as Ω decreases.) A recent calculation of the properties of the low-lying electronic states has been carried out by Tanaka, Sekiya, & Yoshimine (2001).

More recent laboratory work on FeH includes the estimation of the dissociation energy as 1.59 ± 0.08 eV (at 0 K) by Schultz & Armentrout (1991) and the calculation of the first rotational transition $J = 9/2 \leftarrow 7/2$ ($v'' = 0$, $X\ ^4\Delta_{7/2}$) at 1411.0927 GHz (*a*–*a*) and 1411.3579 GHz (*b*–*b*) on the basis of pure rotational laser magnetic resonance spectroscopy in the far-infrared region (Brown, Beaton, & Evenson 1993). The ground $X\ ^4\Delta_i$ state has anomalously large Λ-doubling, presumably as a result of the interaction with the nearby $A\ ^4\Pi$ state some 1200 cm^{-1} above (Langhoff & Bauschlicher 1990). Phillips et al. (1987) chose to follow the Brown et al. (1975) recommendation of using the label *a* for the lower energy level of a Λ doublet and *b* for the upper level when the actual *e*/*f* parity label could not be ascertained. We will also adopt this *a*/*b* labeling scheme. J. Brown (2003, private communication) has, in fact, been able to determine the absolute parity in the ground state, and he finds that *e* lies below *f* for all four spin components (i.e., $a = e$ and $b = f$).

The mid-infrared laser magnetic resonance spectra of FeH were recorded by Towle et al. (1993), and they improved on a few of the predicted line positions (Phillips & Davis 1988) of the 1–0 vibration-rotation band of the $X\ ^4\Delta_{7/2}$ spin component. Phillips et al. (1987) provided a list of term values for $v = 0$, 1, and 2 of the $F\ ^4\Delta_i$ and $X\ ^4\Delta_i$ states determined from an Åslund term value analysis of the line positions. These term values were confirmed by Towle et al. (1993) to have an accuracy of $\pm 0.02\ cm^{-1}$.

The infrared spectrum of FeH (along with FeH_2 and FeH_3) in an argon matrix was recorded by Chertihin & Andrews (1995). Evidently, the earlier matrix measurements by Dendramis, Van Zee, & Weltner (1979) were of FeH_2 and not of FeH.

In addition to the $F\ ^4\Delta_i$–$X\ ^4\Delta_i$ transition, FeH has visible electronic transitions in the blue (4920 Å) and green (5320 Å; Carroll & McCormack 1972; Carroll et al. 1976) that probably also occur in sunspots. However, these FeH lines are heavily blended in the sunspot spectrum, in contrast to the Wing-Ford band. Brown and coworkers (for example, Wilson & Brown 1999, 2001; Hullah, Barrow, & Brown 1999) have devoted much time to the analysis of the visible spectra of FeH using high-resolution dye lasers and a much cooler (450 K) source of molecules. Some of the visible bands (e.g., Hullah et al. 1999) connect to the ground state and improve and extend a few of the term values of Phillips et al. (1987).

2. AB INITIO CALCULATION OF BAND STRENGTHS

The experimental measurement of the radiative lifetime of the Wing-Ford band is difficult mainly because 1 μm is not a convenient wavelength and FeH is difficult to make in the laboratory. In the absence of experimental work, we chose to calculate the transition dipole moment function from the wave functions obtained by ab initio solution of the electronic Schrödinger equation.

The orbitals are determined using a state-averaged complete active space self-consistent field (SA-CASSCF) approach that includes symmetry and equivalence restrictions. In C_{2v} symmetry, the active space contains six a_1 orbitals and one orbital each of b_1, b_2, and a_2 symmetry. This active space includes the Fe 3*d*, 4*s*, and 4*p*σ orbitals, the H 1*s* orbital, and one extra σ orbital, which is added on the basis of preliminary calculations. The three lowest $^4\Delta$ states are included in the SA-CASSCF approach. The third state is added to smooth the potentials and transition moment at larger *r*-values. While the addition of the third state improves the description at large *r*-values, it makes only a very small difference in the final potential at shorter *r*-values. More extensive correlation is included using the multireference configuration interaction (MRCI) approach. These MRCI calculations are performed in C_{2v} symmetry for the four lowest states, which include the three $^4\Delta$ states and a low-lying $^4\Sigma^-$ that is in the same C_{2v} representation.

The MRCI calculations use all CASSCF configurations as reference configurations, and internal contraction (IC; Werner & Knowles 1988; Knowles & Werner 1988) is used to limit the size of the calculations. The importance of higher excitations is estimated using the multireference analog of the Davidson correction, which is denoted +Q. The inclusion of Fe 3*s* and 3*p* correlation did not significantly improve the potentials and, therefore, is not included in the final calculation that correlates the Fe 3*d* and 4*s* and H 1*s* electrons. Scalar relativistic effects are included using the one-electron Douglas Kroll (DK) approach (Hess 1986).

The Fe basis set can be described as (20*s*15*p*10*d*6*f*4*g*)/[7*s*7*p*5*d*3*f*2*g*]. The primitive set is derived from that of Partridge (1989). The *s*, *p*, and *d* primitives are contracted based on a DK-SCF calculation of the ^5D state of Fe atom. The inner 16 *s* primitives are contracted to three functions, and the outermost four are uncontracted; the inner 10 *p* primitives are contracted to two functions, and the outermost five are uncontracted; and the inner six *d* primitives are contracted to one function, and the outermost four are uncontracted. The *f* and *g* sets are taken from our averaged atomic natural orbital set (Bauschlicher 1995). For hydrogen, the augmented correlation consistent polarized valence triple zeta (aug-cc-pVTZ) set (Dunning 1989; Kendall, Dunning, & Harrison 1992) is used, but the contraction coefficients are taken from a DK-SCF calculation. The CASSCF/IC-MRCI calculations are performed using MOLPRO (Werner & Knowles 2002).

The computed IC-MRCI+Q spectroscopic constants are tabulated in Table 1. The IC-MRCI+Q results are in

TABLE 1
SUMMARY OF IC-MRCI+Q SPECTROSCOPIC CONSTANTS, IN cm^{-1}

Parameter	B_0	ω_e	$\omega_e x_e$	T_0
Ground State				
IC-MRCI+Q.....	6.6880	1792.8	35.9	
Expt[a].....	6.50907	1831.80	34.86	
Excited State				
IC-MRCI+Q.....	5.7019	1543.3	31.4	9219.0
Expt.....	5.86663	1501.55	37.80	9995.76
Shifted Potentials				
	B_0	B_1	B_2	
Ground state.....	6.5092	6.1359	5.7809	
Excited state.....	5.8667	5.5071	5.1690	

[a] Present work, averaged over the Λ-doublet components.

reasonable agreement with present experimental values (derived below). Since it is difficult to perform a more accurate calculation and the Rydberg-Klein-Rees (RKR) potentials developed from the experimental constants have problems with the inner wall at relatively low energies, we combine the computed results with experiment to develop our final potentials. We shift the computed potentials so that the computed B_0 values agree with experiment: the ground state is shifted to longer r by 0.0218 Å and the excited state to shorter r by 0.0270 Å. The upper state is shifted up in energy so that the computed T_0 value agrees with the experimental (7/2–7/2) 0–0 band origin. We then generate RKR potentials using the computed B_0, B_1, and B_2 values from the shifted potentials and the experimental ω_e and $\omega_e x_e$ values (averaged over the two Λ-doublet components). Using these RKR potentials and the IC-MRCI transition moment, we evaluate the Franck-Condon factors and Einstein A-values (see Table 2).

TABLE 2
THE EINSTEIN A-VALUES, FRANCK-CONDON FACTORS, AND ENERGY DIFFERENCES

v'	v''	FC	ΔE (cm^{-1})	A (s^{-1})
0.....	0	0.8338	9995.8	0.1018(+7)
0.....	1	0.1616	8226.2	0.9371(+5)
0.....	2	0.0045	6526.4	0.8730(+3)
0.....	3	0.0001	4898.7	0.9800(+1)
0.....	4	0.0000	3345.0	0.1529(+0)
1.....	0	0.1349	11422.3	0.2772(+6)
1.....	1	0.5471	9652.7	0.5721(+6)
1.....	2	0.3015	7952.9	0.1506(+6)
1.....	3	0.0159	6325.2	0.2669(+4)
1.....	4	0.0005	4771.5	0.3059(+2)
2.....	0	0.0234	12771.0	0.7185(+5)
2.....	1	0.2104	11001.5	0.3724(+6)
2.....	2	0.3199	9301.6	0.2808(+6)
2.....	3	0.4082	7673.9	0.1728(+6)
2.....	4	0.0366	6120.2	0.5135(+4)
3.....	0	0.0053	14041.6	0.2224(+5)
3.....	1	0.0558	12272.0	0.1481(+6)
3.....	2	0.2365	10572.2	0.3569(+6)
3.....	3	0.1563	8944.5	0.1112(+6)
3.....	4	0.4741	7390.8	0.1665(+6)
4.....	0	0.0015	15234.2	0.8446(+4)
4.....	1	0.0159	13464.7	0.5823(+5)
4.....	2	0.0876	11764.8	0.1983(+6)
4.....	3	0.2256	10137.1	0.2873(+6)
4.....	4	0.0541	8583.4	0.2830(+5)

3. CALCULATING HÖNL-LONDON FACTORS FOR A $^4\Delta$–$^4\Delta$ TRANSITION

Rotational line strength factors are needed to compute the individual line intensities. Because none are available in the literature for a $^4\Delta$–$^4\Delta$ transition, we have derived the Hönl-London factors (HLFs) needed.

The elements of an electric dipole transition matrix **T** for a Hund's case (a) $\Lambda' S' \Sigma' J' M' \Omega' \rightarrow \Lambda S \Sigma J M \Omega$ rotational transition in the absence of external fields can be expressed in terms of compact spherical tensor notation as

$$\langle \Lambda' S' \Sigma' J' M' \Omega' | \mathbf{T} | \Lambda S \Sigma J M \Omega \rangle = (-1)^{J'-\Omega'} \begin{pmatrix} J' & 1 & J \\ -\Omega' & q & \Omega \end{pmatrix} \times \langle \Lambda' \| \boldsymbol{\mu} \| \Lambda \rangle \delta(S, S') \delta(\Sigma, \Sigma') \delta(M, M') \ . \quad (1)$$

Here $\boldsymbol{\mu} = -e\boldsymbol{r}$ is the electric dipole operator and for case (a) coupling $\Omega = \Lambda + \Sigma$. The presence of the delta functions for S and Σ occurs because $\boldsymbol{\mu}$ does not depend on electron-spin coordinates. The delta functions and the conditions for a nonzero Wigner 3-j symbol establish the well-known case (a) selection rules for allowed transitions:

$$\Delta S = \Delta\Sigma = 0 \ ,$$
$$\Delta\Omega = -q = 0, \ \pm 1 \ ,$$
$$\Delta J = -1(P\text{-branch}), \ 0(Q\text{-branch}), \ +1(R\text{-branch}) \ .$$

The factor $\langle \Lambda' \| \boldsymbol{\mu} \| \Lambda \rangle$ is a constant for a given $\Lambda' \rightarrow \Lambda$ transition. The only real importance of this factor here is that it establishes the selection rule, $\Delta\Lambda = 0, \pm 1$, as a result of the fact that $\boldsymbol{\mu}$ is a rank-one spherical tensor. Furthermore, $\Delta\Omega = \Delta\Lambda + \Delta\Sigma$, and since $\Delta\Sigma = 0$, the selection rule for spin component transitions is reduced simply to $\Delta\Omega = \Delta\Lambda$.

The remaining property to fully characterize case (a) rotational levels is parity. In recent decades, the e/f parity scheme has become the conventionally accepted method by molecular spectroscopists for parity labeling the case (a) rotational levels. The transition matrix in the e/f parity basis is obtained by the transformation

$$\mathbf{U}^\dagger \mathbf{T} \mathbf{U} \ , \quad (2)$$

where **U** is the Wang matrix,

$$U_{ij} = \begin{cases} -\dfrac{1}{\sqrt{2}} & \text{for } j = i < \dfrac{n}{2} \ , \\ +\dfrac{1}{\sqrt{2}} & \text{for } j = i > \dfrac{n}{2} \ , \\ +1 & \text{for } j = i = \dfrac{n}{2} \ , \\ +\dfrac{1}{\sqrt{2}} & \text{for } j = n - i + 1 \ , \\ 0 & \text{otherwise} \ , \end{cases} \quad (3)$$

with n being the total number of $\Lambda S \Sigma$ states. For P- and R-branch lines the resultant matrix is partitioned into two nonzero diagonal blocks of equal dimension, where one

TABLE 3
$^4\Delta$–$^4\Delta$ Hönl-London Factors: Hund's Case (a) Coupling

Branch	Ω''	Parity	Ω'	Parity	$S(J)$
$P(J)$	7/2	e/f	7/2	e/f	$(1/4)[(2J-7)(2J+7)/J]$
	5/2	e/f	5/2	e/f	$(1/4)[(2J-5)(2J+5)/J]$
	3/2	e/f	3/2	e/f	$(1/4)[(2J-3)(2J+3)/J]$
	1/2	e/f	1/2	e/f	$(1/4)[(2J-1)(2J+1)/J]$
$Q(J)$	7/2	e/f	7/2	f/e	$(49/4)[(2J+1)/J(J+1)]$
	5/2	e/f	5/2	f/e	$(25/4)[(2J+1)/J(J+1)]$
	3/2	e/f	3/2	f/e	$(9/4)[(2J+1)/J(J+1)]$
	1/2	e/f	1/2	f/e	$(1/4)[(2J+1)/J(J+1)]$
$R(J)$	7/2	e/f	7/2	e/f	$(1/4)[(2J-5)(2J+9)/(J+1)]$
	5/2	e/f	5/2	e/f	$(1/4)[(2J-3)(2J+7)/(J+1)]$
	3/2	e/f	3/2	e/f	$(1/4)[(2J-1)(2J+5)/(J+1)]$
	1/2	e/f	1/2	e/f	$(1/4)[(2J+1)(2J+3)/(J+1)]$

block corresponds to $e \rightarrow e$ transitions and the other to $f \rightarrow f$. In contrast, the transition matrix for the Q-branch lines in the parity basis is comprised of two nonzero off-diagonal blocks, the $e \rightarrow f$ and the $f \rightarrow e$ transitions.

Results for the $^4\Delta$–$^4\Delta$ transition ($\Omega' = \Omega = \frac{1}{2}$, 3/2, 5/2, 7/2) are displayed in Table 3. Apart from the constant factor $\langle \Delta \| \boldsymbol{\mu} \| \Delta \rangle$, the HLFs, designated by $S(J)$, are the squares of the matrix elements of $\mathbf{U}^{\dagger}\mathbf{T}\mathbf{U}$.

Because Hund's case (a) and case (b) are both well-defined coupling schemes, that is, the coupling does not depend on molecular parameters, it then becomes a matter of just simply constructing a transformation matrix $\mathbf{U}$ in closed analytical form where $\mathbf{U}^{\dagger}\mathbf{T}\mathbf{U}$ converts $\mathbf{T}$ in the case (a) nonparity basis over to case (b), or vice versa. The matrix elements for such a transformation are

$$\begin{aligned}\langle \Lambda S \Sigma J M \Omega | \Lambda N \Lambda S J M \rangle &= \langle \Lambda N \Lambda S J M | \Lambda S \Sigma J M \Omega \rangle \\ &= (-1)^{S-N+\Omega}\sqrt{2N+1} \\ &\quad \times \begin{pmatrix} J & S & N \\ -\Omega & \Sigma & \Lambda \end{pmatrix}. \end{aligned} \tag{4}$$

The case (b) HLFs in Table 4 were derived using this approach.

For case (b) coupling, Σ and Ω are no longer defined, whereas Λ is a well-defined quantum number for both coupling cases. Secondly, rotational energies for case (a) are computed using the Hamiltonian operator $B(r)\mathbf{R}^2$, where

TABLE 4
$^4\Delta$–$^4\Delta$ Hönl-London Factors: Hund's Case (b) Coupling

Branch	N''	Parity	N'	Parity	$S(J)$
$^PP(J)$	$J-3/2$	$+/-$	$J-5/2$	$+/-$	$(1/4)[(2J-7)(2J+1)^2/(2J-3)(J-1)]$
$^QP(J)$	$J-3/2$	$+/-$	$J-3/2$	$+/-$	$48[(2J+1)/J(2J-3)(2J-1)^2]$
$^RP(J)$	$J-3/2$	$+/-$	$J-1/2$	$+/-$	$(3/4)[(2J-5)(2J+3)/J^2(2J-1)^2(J-1)]$
$^PP(J)$	$J-1/2$	$+/-$	$J-3/2$	$+/-$	$(1/4)[(2J-5)(2J-3)(2J+1)(2J+3)(J+1)/J^2(2J-1)^2]$
$^QP(J)$	$J-1/2$	$+/-$	$J-1/2$	$+/-$	$256[(J-1)(J+1)/J(2J-1)^2(2J+1)^2]$
$^RP(J)$	$J-1/2$	$+/-$	$J+1/2$	$+/-$	$(3/4)[(2J-3)(2J+5)/J^2(2J+1)^2(J+1)]$
$^PP(J)$	$J+1/2$	$+/-$	$J-1/2$	$+/-$	$(1/4)[(2J-3)(2J-1)(2J+3)(2J+5)(J-1)/J^2(2J+1)^2]$
$^QP(J)$	$J+1/2$	$+/-$	$J+1/2$	$+/-$	$48[(2J-1)/J(2J+1)^2(2J+3)]$
$^PP(J)$	$J+3/2$	$+/-$	$J+1/2$	$+/-$	$(1/4)[(2J-1)^2(2J+7)/(2J+3)(J+1)]$
$^QQ(J)$	$J-3/2$	$+/-$	$J-3/2$	$+/-$	$16[(2J+1)(J+1)/J(2J-1)^2]$
$^RQ(J)$	$J-3/2$	$+/-$	$J-1/2$	$+/-$	$(3/4)[(2J-5)(2J+1)(2J+3)/J^2(2J-1)^2]$
$^PQ(J)$	$J-1/2$	$+/-$	$J-3/2$	$+/-$	$(3/4)[(2J-5)(2J+1)(2J+3)/J^2(2J-1)^2]$
$^QQ(J)$	$J-1/2$	$+/-$	$J-1/2$	$+/-$	$16[(2J^2+J-4)^2/J(2J-1)^2(2J+1)(J+1)]$
$^RQ(J)$	$J-1/2$	$+/-$	$J+1/2$	$+/-$	$(1/4)[(2J-3)(2J-1)(2J+3)(2J+5)/J^2(2J+1)(J+1)^2]$
$^PQ(J)$	$J+1/2$	$+/-$	$J-1/2$	$+/-$	$(1/4)[(2J-3)(2J-1)(2J+3)(2J+5)/J^2(2J+1)(J+1)^2]$
$^QQ(J)$	$J+1/2$	$+/-$	$J+1/2$	$+/-$	$16[(2J^2+3J-3)^2/J(2J+1)(2J+3)^2(J+1)]$
$^RQ(J)$	$J+1/2$	$+/-$	$J+3/2$	$+/-$	$(3/4)[(2J-1)(2J+1)(2J+7)/(2J+3)^2(J+1)^2]$
$^PQ(J)$	$J+3/2$	$+/-$	$J+1/2$	$+/-$	$(3/4)[(2J-1)(2J+1)(2J+7)/(2J+3)^2(J+1)^2]$
$^QQ(J)$	$J+3/2$	$+/-$	$J+3/2$	$+/-$	$16[J(2J+1)/(2J+3)^2(J+1)]$
$^RR(J)$	$J-3/2$	$+/-$	$J-1/2$	$+/-$	$(1/4)[(2J-5)(2J+3)^2/J(2J-1)]$
$^QR(J)$	$J-1/2$	$+/-$	$J-1/2$	$+/-$	$48[(2J+3)/(2J-1)(2J+1)^2(J+1)]$
$^RR(J)$	$J-1/2$	$+/-$	$J+1/2$	$+/-$	$(1/4)[(2J-3)(2J-1)(2J+3)(2J+5)(J+2)/(2J+1)^2(J+1)^2]$
$^PR(J)$	$J+1/2$	$+/-$	$J-1/2$	$+/-$	$(3/4)[(2J-3)(2J+5)/J(2J+1)^2(J+1)^2]$
$^QR(J)$	$J+1/2$	$+/-$	$J+1/2$	$+/-$	$256[J(J+2)/(2J+1)^2(2J+3)^2(J+1)]$
$^RR(J)$	$J+1/2$	$+/-$	$J+3/2$	$+/-$	$(1/4)[J(2J-1)(2J+1)(2J+5)(2J+7)/(2J+3)^2(J+1)^2]$
$^PR(J)$	$J+3/2$	$+/-$	$J+1/2$	$+/-$	$(3/4)[(2J-1)(2J+7)/(2J+3)^2(J+1)^2(J+2)]$
$^QR(J)$	$J+3/2$	$+/-$	$J+3/2$	$+/-$	$48[(2J+1)/(J+1)(2J+3)^2(2J+5)]$
$^RR(J)$	$J+3/2$	$+/-$	$J+5/2$	$+/-$	$(1/4)[(2J+1)^2(2J+9)/(2J+5)(J+2)]$

$\mathbf{R} = \mathbf{J} - \mathbf{L} - \mathbf{S}$. For case (b) the Hamiltonian operator is $B(r)\mathbf{N}^2$, where $\mathbf{N} = \mathbf{R} + \mathbf{L} = \mathbf{J} - \mathbf{S}$. Thus, for a given J-value and discounting parity, there are four rotational levels with N-values, $J - 3/2$, $J - \frac{1}{2}$, $J + \frac{1}{2}$, and $J + 3/2$ for $S = 3/2$, which equals the number of spin components with Ω-values, $\frac{1}{2}$, $3/2$, $5/2$, and $7/2$ for case (a) coupling. In addition, the e/f parity labeling is not convenient for the case (b) rotational levels since the basis functions $|\Lambda N \Lambda S J M\rangle$ are already eigenfunctions of the parity operator; they are labeled simply as $+$ or $-$ to correspond to the $\pm\Lambda$ degeneracy. For case (b) rotational transitions, the parity selection rules are $+ \rightarrow +$ and $- \rightarrow -$, regardless of whether the branch is P, Q, or R. This $+$ or $-$ orbital parity is written as a right superscript to the term symbol (e.g., $^1\Sigma^+$ or $^4\Delta^+$) and is not to be confused with total parity (Bernath 1995).

These finer points between case (a) and case (b) help to explain the notation differences in Tables 3 and 4. The Ω and parity labels along with the ΔJ P-, Q-, and R-branch designations in Table 3 are sufficient to label uniquely all the allowed case (a) rotational transitions. The quantum number N in case (b) serves as a label analogous to Ω in case (a). In addition to the strong $\Delta N = \Delta J$ transitions, which form the so-called main branches (analogous to the case [a] $\Delta\Omega = \Delta\Lambda$ branches), there also exist weaker $\Delta N \neq \Delta J$ transitions, which account for the better than twofold increase in the number of branches. To distinguish $\Delta N = \Delta J$ from $\Delta N \neq \Delta J$ branches, the traditional convention is to augment the ΔJ P-, Q-, or R-branch designations with ΔN P, Q, or R left superscript designations when $\Delta N \neq \Delta J$. In Table 4 this convention is not strictly followed; to alleviate any confusion, the redundant ΔN superscripts are retained for the main branches as well. Note that in order to avoid errors in the HLFs in Tables 3 and 4, they were generated with the computer algebra program Maple.

For the X and $F\ ^4\Delta$ states of FeH, the coupling is intermediate between case (a) and case (b) for increasing J. To further complicate matters, the rotational levels for both of these states are perturbed by unknown electronic states. The former problem of intermediacy can be treated by constructing the energy Hamiltonian $\mathbf{H}$ in the case (a) basis as shown in Table 5 (see Table 6 for case [b]). The eigenvectors $\mathbf{U}$ from the diagonalization $\mathbf{U}^\dagger\mathbf{H}\mathbf{U}$ for both the lower and upper states l and u are then used to correct the HLFs for intermediate coupling by the process $\mathbf{U}_l^\dagger\mathbf{T}\mathbf{U}_u$.

TABLE 5

$^4\Delta$ Hund's Case (a) Hamiltonian Matrix $x = J + 1/2$

Term	Value
$\langle 7/2\|H\|7/2\rangle$	$T + 3A + 2\lambda + B(x^2 - 7) - D(x^4 - 11x^2 + 22)$
$\langle 7/2\|H\|5/2\rangle$	$\langle 5/2\|H\|7/2\rangle = -[B - 2D(x^2 - 3)]\sqrt{3(x^2 - 9)}$
$\langle 7/2\|H\|3/2\rangle$	$\langle 3/2\|H\|7/2\rangle = -2D\sqrt{3(x^2 - 9)(x^2 - 4)}$
$\langle 7/2\|H\|1/2\rangle$	$\langle 1/2\|H\|7/2\rangle = 0$
$\langle 5/2\|H\|5/2\rangle$	$T + A - 2\lambda + B(x^2 + 1) - D(x^4 + 9x^2 - 42)$
$\langle 5/2\|H\|3/2\rangle$	$\langle 3/2\|H\|5/2\rangle = -2[B - 2D(x^2 + 3)]\sqrt{x^2 - 4}$
$\langle 5/2\|H\|1/2\rangle$	$\langle 1/2\|H\|5/2\rangle = -2D\sqrt{3(x^2 - 4)(x^2 - 1)}$
$\langle 3/2\|H\|3/2\rangle$	$T - A - 2\lambda + B(x^2 + 5) - D(x^4 + 17x^2 + 6)$
$\langle 3/2\|H\|1/2\rangle$	$\langle 1/2\|H\|3/2\rangle = -[B - 2D(x^2 + 5)]\sqrt{3(x^2 - 1)}$
$\langle 1/2\|H\|1/2\rangle$	$T - 3A + 2\lambda + B(x^2 + 5) - D(x^4 + 13x^2 + 22)$

The Phillips et al. (1987) tables of experimental term values for the X and F $v = 0$, 1, and 2 levels were used along with the eigenvalues of $\mathbf{H}$ in least-squares fits to determine the molecular constants, T_v, B_v, D_v, A_v, and λ_v, separately for each parity a and b. (The distinction between e/f and the Phillips et al. a/b labeling is irrelevant as far as the analysis presented here is concerned.) As a result of the perturbations, these fits gave rather disappointing results, yielding standard deviations on the order of 2–4 cm^{-1} for the X levels and 1–3 cm^{-1} for the F levels. To minimize the effects of these perturbations as much as possible, an alternate fitting procedure was tried using the average of the experimental term values for each J-value for the four spin components. The results from these fits showed remarkable improvement with roughly a factor of 10 reduction in the standard deviations, 0.1–0.7 cm^{-1} for the X levels and 0.2–0.4 cm^{-1} for the F levels. Nevertheless, these standard deviations are still a factor of 10 higher than the estimated experimental

TABLE 6

$^4\Delta$ Hund's Case (b) Hamiltonian Matrix

Term	Value
	$x = N = J - 3/2$
$\langle x\|H\|x\rangle$	$T + Bx(x+1) - Dx^2(x+1)^2 + 6A/(x+1) - 2\lambda[(x-3)(x+4)/(x+1)(2x+3)]$
$\langle x\|H\|x+1\rangle$	$\langle x+1\|H\|x\rangle = [A(x+2) + 4\lambda]\sqrt{3(x-1)(x+3)(2x+5)/(x+1)^2(x+2)^2(2x+3)}$
$\langle x\|H\|x+2\rangle$	$\langle x+2\|H\|x\rangle = 2\lambda\sqrt{3(x-1)x(x+3)^2(x+4)/(x+1)(x+2)^2(2x+3)^2}$
$\langle x\|H\|x+3\rangle$	$\langle x+3\|H\|x\rangle = 0$
	$x = N = J - 1/2$
$\langle x\|H\|x\rangle$	$T + Bx(x+1) - Dx^2(x+1)^2 + 2A[(x-3)/x(x+1)] + 2\lambda[(x-3)(x+3)(x+4)/x(x+1)(2x+3)]$
$\langle x\|H\|x+1\rangle$	$\langle x+1\|H\|x\rangle = 4[Ax(x+2) - 6\lambda]\sqrt{(x-1)(x+3)/x(x+1)^2(x+2)(2x+1)(2x+3)}$
$\langle x\|H\|x+2\rangle$	$\langle x+2\|H\|x\rangle = 2\lambda\sqrt{3(x-1)x^2(x+3)(x+4)/(x+1)^2(x+2)(2x+3)^2}$
	$x = N = J + 1/2$
$\langle x\|H\|x\rangle$	$T + Bx(x+1) - Dx^2(x+1)^2 - 2A[(x+4)/x(x+1)] + 2\lambda[(x-3)(x-2)(x+4)/x(x+1)(2x-1)]$
$\langle x\|H\|x+1\rangle$	$\langle x+1\|H\|x\rangle = (Ax - 4\lambda)\sqrt{3(x-1)(x+3)(2x-1)/x^2(x+1)^2(2x+1)}$
	$x = N = J + 3/2$
$\langle x\|H\|x\rangle$	$T + Bx(x+1) - Dx^2(x+1)^2 - 6A/x - 2\lambda[(x-3)(x+4)/x(2x-1)]$

uncertainties of better than 0.05 cm^{-1}, indicating the extent of residual effects due to the perturbations that averaging was unable to remove. Fitting the term values in this manner cannot determine the spin-orbit and spin-spin constants. These A- and λ-values instead were determined in separate fits utilizing the spin-splitting data in Table 6C of Phillips et al. (1987). To within the quoted experimental error of 0.5 cm^{-1}, the spin splittings for all the observed vibrational levels can be reproduced by a single A- and λ-value for each electronic state. The molecular constants in Table 7 represent a marginal improvement over those reported by Phillips et al. (1987), who derived their constants by fitting the rotational line positions to a simple polynomial expression. Our new constants, however, extrapolate somewhat better to higher J- and v-values.

The specified range in temperature for the opacity calculations required extending the spectrum to include rotational lines up to $J'' = J' = 50.5$ and vibrational transitions up to $v'' = v' = 4$. The term values used in generating the spectrum for the low-resolution opacity calculations are listed in Table 8. The entries are a combination of experimental term values taken from the tables of Phillips et al. (1987) and calculated values for the higher v and J levels. The missing entries in their tables for the lower J levels were calculated by simple polynomial extrapolation. Even in spite of the perturbations, the observed term values are surprisingly smooth functions of J. This smoothness was maintained in extending the term values to higher J by averaging the observed to calculated term value ratios in the region of overlap and then multiplying the calculated term values outside the region by this average ratio.

In light of the perturbations, there are obvious concerns regarding the reliability of the HLFs for intermediate coupling (Table 3 or Table 4) using either the case (a) Hamiltonian model in Table 5 or case (b) model in Table 6. To address this issue, we did a comparison of the HLFs with the measured line intensities from a McMath-Pierce FTS archived emission spectrum recorded on 1984 May 23 at a furnace temperature of 2350°C and a background pressure of 70 torr. This spectrum was then ratioed to the archived companion Optronics reference lamp spectrum to remove the variation of detector response with wavenumber from the background signal. The bands specifically targeted for this comparison were the $\Delta v = 0$ and -1 bands involving

TABLE 7
MOLECULAR CONSTANTS FOR THE $X\,^4\Delta$ AND $F\,^4\Delta$ STATES

Parameter	$v = 0$	$v = 1$	$v = 2$
$X\,^4\Delta$ State [$A = -116.860(524)$, $\lambda = 10.645(693)$]			
Parity a			
T_v	315.879(221)	2078.171(358)	3769.400(361)
B_v	6.49504(312)	6.29867(516)	6.16724(471)
D_v	0.00022624(833)	0.0000592(139)	0.0001586(136)
ω_e	1833.36(113)		
$\omega_e x_e$	35.53(50)		
B_e	6.5662(185)		
α_e	0.1639(108)		
Parity b			
T_v	319.5395(458)	2081.421(627)	3774.95(134)
B_v	6.523101(590)	6.34794(918)	6.1016(226)
D_v	0.00023866(143)	0.0001967(261)	−0.0001767(800)
ω_e	1830.23(189)		
$\omega_e x_e$	34.18(80)		
B_e	6.6403(203)		
α_e	0.2108(119)		
$F\,^4\Delta$ State [$A = -124.816(692)$, $\lambda = -9.263(916)$]			
Parity a			
T_v	10313.114(186)	11737.011(440)	13085.964(591)
B_v	5.87584(210)	5.69283(553)	5.45930(847)
D_v	0.00040430(421)	0.0004711(138)	0.0004365(249)
ω_e	1498.84(145)		
$\omega_e x_e$	37.47(60)		
B_e	5.9884(147)		
α_e	0.20827(842)		
Parity b			
T_v	10313.819(225)	11741.817(195)	13093.571(481)
B_v	5.85742(290)	5.60903(264)	5.38113(718)
D_v	0.00032849(704)	0.00034484(684)	0.0002624(204)
ω_e	1504.24(80)		
$\omega_e x_e$	38.12(40)		
B_e	5.97308(583)		
α_e	0.23815(342)		

TABLE 8
THE $X\ ^4\Delta$ $v = 0$ TERM VALUES

	7/2		5/2		3/2		1/2	
J	a	b	a	b	a	b	a	b
0.5.....	...	...	...	...	...	...	694.40	699.70
1.5.....	...	...	...	...	450.60	450.92	716.44	723.28
2.5.....	...	...	244.68	244.68	484.89	486.22	753.10	762.42
3.5.....	80.70	80.70	288.71	288.82	532.71	535.37	805.18	816.01
4.5.....	127.77	127.78	345.10	345.52	593.88	598.64	872.65	883.92
5.5.....	186.02	186.02	413.74	414.70	668.52	675.70	955.21	965.98
6.5.....	255.66	255.77	494.53	496.41	756.52	766.33	1052.62	1062.02
7.5.....	336.97	337.20	587.45	590.63	857.95	870.28	1164.51	1171.98
8.5.....	430.13	430.59	692.50	697.42	972.76	987.31	1290.54	1295.71
9.5.....	535.29	536.07	809.71	816.74	1100.98	1117.20	1430.42	1433.13

NOTE.—Table 8 is published in its entirety in the electronic edition of the *Astrophysical Journal*. A portion is shown here for guidance regarding its form and content.

the main $\Delta\Omega = 0$ branches versus the $\Delta\Omega = \pm 1$ satellite branches. Rotational line intensities in these bands were measured by fitting the observed rotational line shapes to a Voigt line shape function preceded by subtraction of the background signal level in the vicinity of line center to determine absolute peak intensities. Measured rotational line intensities in the satellite branches were for the most part a factor of 6 times weaker than the corresponding ones in the main branches that shared common upper levels. The calculated line strength factors based on the Table 5 or Table 6 Hamiltonian model predict on the other hand that the ratio of these satellite to main branch lines should be weaker by a factor more like 70 for the low-J lines ($J'' \sim 3.5$) and 50 for the high-J lines ($J'' \sim 50.5$). Obviously the F and X states are not pure $^4\Delta$ states.

4. GENERATION OF LINE LISTS

The line positions for the $F\ ^4\Delta_i$–$X\ ^4\Delta_i$ transition for $v = 0$–4 and $J \leq 50.5$ were generated from term values in Table 8. All possible lines were computed consistent with the electric dipole selection rules for J ($\Delta J = 0, \pm 1$) and parity (a–a, b–b for R- and P-branches and a–b, b–a for Q-branches). For Hund's case (a) coupling there are only two strong branches (P and R) and a Q-branch whose intensity decreases rapidly with J (Table 3) for each spin component (12 branches in total). For Hund's case (b), numerous satellite branches appear, and there are 28 branches in all.

The Einstein A-values for each line were computed using the formula $A = A_{v'v''}\mathrm{HLF}/(2J' + 1)$, in which the Einstein A for the v'–v'' band is taken from Table 2 and the HLF is computed as discussed above. Because the F–X transition of FeH is intermediate between Hund's cases (a) and (b), the HLFs were calculated from the Hund's case (a) HLFs and the eigenvectors used to diagonalize the Hamiltonian matrix. Note that at high J these calculated factors are nearly identical with those given by the Hund's case (b) formula in Table 4. The individual Einstein A-values for each rovibronic line can be converted to dimensionless gf-values with the formula

$$gf = (2J'' + 1)f_{\mathrm{abs}} = \frac{\epsilon_0 m_e c^3}{2\pi e^2 \nu^2} A(2J' + 1) \ , \qquad (5)$$

using SI units.

The line positions and line intensities were collected into 25 files, one for each of the bands involving v' and v'' 0–4 and for P-, Q-, and R-branches. These files can be obtained on-line.[6]

5. CALCULATION OF FeH OPACITIES

As with the molecule CrH (Burrows et al. 2002), the integrated line strengths were computed from input Einstein A-coefficients obtained from the calculated line lists. Since the A-coefficients already include all the details of the line strength, i.e., the strength of the associated band and its Franck-Condon factor, as well as the individual HLF, these factors do not need to be considered separately. As in Burrows et al. (2002), the integrated line strength in $\mathrm{cm^2\ s^{-1}}$ $\mathrm{molecule^{-1}}$ is calculated from

$$S = \frac{1}{8\pi\bar{\nu}^2} \frac{A(2J' + 1)\exp(-E''hc/kT)[1 - \exp(-hc\bar{\nu}/kT)]}{Q} \ , \qquad (6)$$

where J' is the upper rotational quantum number, $\bar{\nu}$ is the transition wavenumber in $\mathrm{cm^{-1}}$, E'' is the excitation energy of the lower state in $\mathrm{cm^{-1}}$, and Q is the internal partition function. The stimulated emission factor is also included in equation (6). Note that there is a small error in the Burrows et al. (2002) equation for S and the correct version has $2J' + 1$, not $2J'' + 1$. The reason for this change is that an extra factor of $(2J' + 1)/(2J'' + 1)$ is needed to convert the emission quantity A to the absorption quantity S.

The monochromatic cross section per molecule is obtain by multiplying the value from equation (6) by a truncated Lorentzian profile. A simple prescription provided by R. Freedman (2000, private communication) is used to calculate the J-dependent FWHM in $\mathrm{cm^{-1}}$ of a line given by

$$\Delta\bar{\nu} = [W_a - W_b \min(J'', 30)]P_{\mathrm{atm}} \ ,$$

where W_a and W_b are line broadening coefficients, with the values 0.15 and 0.002, respectively, J'' is the rotational quantum number of the lower state, and P_{atm} is the total gas pressure in atmospheres. This simple prescription causes the

[6] See http://bernath.uwaterloo.ca/FeH.

lines to decrease in width up to $J'' = 30$ and thereafter remain at a constant width.

The line is profiled using a Lorentzian function on a spectral grid with a 1 cm^{-1} grid spacing. In order to save computer time and to simulate the rapid drop-off in intensity in the far wings, the profile is truncated beyond $\Delta\bar{\nu}_{\rm trunc}$ cm^{-1} from the line center, where $\Delta\bar{\nu}_{\rm trunc}$ is the smaller of $25P_{\rm atm}$ and 100, so a profile is never computed more than 100 cm^{-1} on either side of the line center. However, in order to conserve the total line strength, a normalizing factor is applied to the profile.

At very low pressures, the lines may be so narrow that they may "fall between" the grid points and be undersampled or missed completely. To ensure that the lines are properly represented, the line centers are moved to the nearest grid point, regardless of the width, and then for very narrow lines where only the grid point at the line center is represented, the line is artificially broadened to include the two neighboring grid points and normalized so that the area covered corresponds to the total line strength.

The internal partition function (Q) is calculated from all electronic molecular states for which experimental and theoretical information is available and that make a significant contribution for the temperatures of relevance. This includes the ground ($X\,^4\Delta$) and excited ($F\,^4\Delta$) states that produce the band systems being computed, as well as eight intermediate excited states that lie below the F state. Of these 10 states, we have estimated the excitation energies of the spin-split substates for the first five. The energy levels and spectroscopic constants used in the calculation of Q are provided in Tables 9 and 10.

Associated with each of the 10 electronic states are the vibrational and rotational constants ω_e, $\omega_e x_e$, B_e, and D_e, where it is assumed that for all spin-split substates belonging to an electronic state the constants are the same. Normally for partition functions this is a good approximation. The individual partition function for the electronic state i is given by the product $Q_{e_i} \times Q_{v_i} \times Q_{r_i}$, which are, respectively, the electronic, vibrational, and rotational partition functions. Q_{e_i} is a small integer depending on electron spin and orbital angular momentum, and Q_{v_i} and Q_{r_i} are calculated using asymptotic formulae from Kassel (1933a, 1933b). The total internal partition function is calculated by summing up the individual electronic states weighed by the Boltzmann factor using

$$Q = \sum_{i=1}^{n} Q_{e_i} Q_{v_i} Q_{r_i} \exp\left(-\frac{T_i hc}{kT}\right), \qquad (7)$$

where T_i is the excitation energy of state i and is zero for the ground state ($i = 1$). The computed partition function from 1000 to 3500 K in 100 K increments is provided in Table 11. As a test we computed the function by direct summation of the X and F state energy levels used to generate the line list. The partition function was also computed using the analytical formulae (cited above) using all of the low-lying electronic states (Tables 9 and 10). These low-lying electronic states make an important contribution to Q (Table 11) at all relevant temperatures and should not be neglected.

In order to calculate the abundance of FeH at a particular temperature and pressure in model calculations assuming chemical equilibrium, the free energy of FeH is calculated at the temperature in question, and then the total free energy of the system is minimized (Sharp & Huebner 1990). However, this requires up-to-date thermodynamic data. Accordingly, these were calculated from the partition function of FeH using equation (7) with our new data, the partition functions of the dissociated atoms Fe and H, and the dissociation energy of FeH (taken as 1.598 eV). It was found that the partition function calculated with our new data was about a factor of 2 larger than the old value.

Along with the most abundant isotope (^{56}Fe, which makes up 91.7% of iron), ^{54}Fe, ^{57}Fe, and ^{58}Fe are included and make up 5.8%, 2.2%, and 0.28%, respectively. The corresponding vibrational, rotational, and vibration-rotation coupling constants for any isotopically substituted molecule of FeH can be obtained from the ratio of the reduced mass

TABLE 9
FeH Energy Levels for Thermochemistry

State	Term Value (cm^{-1})
$X\,^4\Delta_{7/2}$	0
$X_{5/2}$	191
$X_{3/2}$	426
$X_{1/2}$	695
$A\,^4\Pi_{5/2}$	910
$A_{3/2}$	1068
$A_{1/2}$	1228
$A_{-1/2}$	1388
$a\,^6\Delta_{9/2}$	1766
$a_{7/2}$	1981
$a_{5/2}$	2177
$a_{3/2}$	2356
$a_{1/2}$	2518
$a_{-1/2}$	2656
$C\,^4\Phi_{9/2}$	3174
$C_{7/2}$	3375
$C_{5/2}$	3575
$C_{3/2}$	3735
$b\,^6\Pi_{7/2}$	3889
$b_{5/2}$	3939
$b_{3/2}$	3989
$b_{1/2}$	4039
$b_{-1/2}$	4089
$b_{-3/2}$	4139
$c\,^6\Sigma^+$	4750
$B\,^4\Sigma^-$	5089
$D\,^4\Sigma^+$	7158
$E\,^4\Pi$	7300
$F\,^4\Delta$	9995

TABLE 10
FeH Constants for Thermochemistry in cm^{-1}

State	B_e	α_e	D_e	ω_e	$\omega_e x_e$
$X\,^4\Delta$	6.5906	0.2116	8.5×10^{-5}	1826.86	31.96
$A\,^4\Pi$	6.86	0.22	1×10^{-4}	1875	34
$a\,^6\Delta$	6.00	0.2	1.4×10^{-4}	1680	30
$C\,^4\Phi$	6.6	0.2	1×10^{-4}	1680	30
$b\,^6\Pi$	5.9	0.2	1×10^{-4}	1600	30
$c\,^6\Sigma^+$	6.7	0.2	1×10^{-4}	1600	30
$B\,^4\Sigma^-$	6.9	0.2	1×10^{-4}	1875	34
$D\,^4\Sigma^+$	6.5	0.2	1×10^{-4}	1800	30
$E\,^4\Pi$	6.86	0.22	1×10^{-4}	1875	34
$F\,^4\Delta$	5.936	0.19	1×10^{-4}	1498	37

TABLE 11
PARTITION FUNCTION OF FeH BY LEVEL SUMMATION AND ANALYTIC EVALUATION (SEE TEXT)

T (K)	Summation	Analytic
1000	6.97184E+02	8.89514E+02
1100	8.03851E+02	1.08709E+03
1200	9.17504E+02	1.31250E+03
1300	1.03828E+03	1.56785E+03
1400	1.16627E+03	1.85520E+03
1500	1.30158E+03	2.17658E+03
1600	1.44427E+03	2.53392E+03
1700	1.59438E+03	2.92912E+03
1800	1.75196E+03	3.36400E+03
1900	1.91703E+03	3.84032E+03
2000	2.08960E+03	4.35980E+03
2100	2.26969E+03	4.92408E+03
2200	2.45731E+03	5.53478E+03
2300	2.65244E+03	6.19343E+03
2400	2.85509E+03	6.90156E+03
2500	3.06524E+03	7.66062E+03
2600	3.28289E+03	8.47207E+03
2700	3.50803E+03	9.33728E+03
2800	3.74062E+03	1.02576E+04
2900	3.98065E+03	1.12344E+04
3000	4.22809E+03	1.22691E+04
3100	4.48291E+03	1.33627E+04
3200	4.74507E+03	1.45167E+04
3300	5.01453E+03	1.57323E+04
3400	5.29123E+03	1.70107E+04
3500	5.57513E+03	1.83531E+04

of that molecule and the reduced mass of $^{56}Fe^{1}H$. These constants depend on various $\frac{1}{2}$-integer powers of the ratio of reduced masses, as given by Herzberg (1950). From the vibrational and rotational quantum numbers of the upper and lower states for each transition, the isotopic shifts of the lines are computed. The strength of each line is calculated by applying the fraction of the isotope of iron to equation (6). To calculate the cross section as a function of frequency, this is then multiplied by the abundance of FeH and the profile.

Because of the isotopic shifts of the energy levels, the partition function and the Boltzmann factor of the lower states will be affected, which will have a small effect on the line strengths. Likewise, there will be a small effect due to a changed oscillator strength caused by a shift in the frequency of the transition, and slightly changed wave functions will alter the Franck-Condon factors. All these effects are very small compared with the shifting of the lines, and so they are ignored. The shifted lines may be important as they could fill in gaps in the $^{56}Fe^{1}H$ opacity spectrum.

The whole process is repeated for each of the 25 bands of FeH considered for all possible combinations of the upper and lower vibrational quantum numbers taking values between 0 and 4 and for each of the four isotopic versions; thus, 100 bands are calculated.

6. REPRESENTATIVE FeH OPACITY PLOTS AND A THEORETICAL L DWARF SPECTRUM

Using the procedure outlined in § 5, we have calculated tables of FeH opacities for a broad range of the temperatures and pressures encountered in L and T dwarf atmospheres. These opacities have also been incorporated, along with the new FeH abundances, into a spectral synthesis code (Burrows et al. 2002) used to derive theoretical spectra and colors for cool, often substellar, objects with molecular atmospheres. A representative opacity spectrum at a temperature of 1800 K and a pressure of 30 atm for wavelengths from $\sim$0.65 to $\sim$1.6 μm for both FeH and CrH (Burrows et al. 2002) is provided in Figure 1. The new FeH opacities are $\sim$100 times larger than those found in Schiavon et al. (1997). The CrH opacities are presented along with the new FeH opacities to demonstrate the similarities and differences between the opacities for the two molecules. The Wing-Ford band of FeH near $\sim$0.99 μm is accompanied by a similar band for CrH. In addition, the prominent FeH 1–0 band feature near 0.87 μm is accompanied by a CrH feature near 0.86 μm. Importantly, the J photometric band between 1.19 and 1.30 μm boasts lines from both molecules, although previously only FeH features have been identified. Figure 2 focuses on the J band and has a resolution near 0.22 cm^{-1}. Clearly both molecules must be considered when analyzing high-resolution spectra in this band.

Figure 3 portrays a comparison between the L5 dwarf 2MASS-1507 (Kirkpatrick et al. 1999b) and a solar-metallicity theoretical spectrum at 0.85 μm to $\sim$1.0 μm, calculated using the new FeH and CrH (Burrows et al. 2002) opacities and abundances. An effective temperature of 1700 K and a gravity of $10^{4.5}$ cm s^{-2} were assumed, and the new solar elemental abundances from Allende-Prieto, Lambert, & Asplund (2002) for oxygen and carbon were used. The latter decrease the depth of the water feature near 0.94 μm and lead to a better fit in that region of the spectrum than could previously be obtained. The theoretical model was offset for clarity of comparison with the data. Since 2MASS-1507 is an L dwarf, silicate clouds figure prominently in their atmospheres (Burrows et al. 2001). We have incorporated a forsterite cloud with 50 μm particles that sequesters 10% of the solar magnesium. Such a cloud, while having an important effect in the J, H, and K bands, does not dominate the depicted spectrum. Clearly, the FeH and CrH features around the Wing-Ford band and near the 0.86/0.87 μm features are reasonably reproduced, along with the overall spectral slope. The fit is improved just longward of 0.87 μm as a result of the inclusion of the FeH opacities redward of the band head. The relative strengths of the paired FeH and CrH features depicted seem good, although playing with the abundances, effective temperature, cloud model, and gravity could no doubt further improve the fit.

Figure 3 demonstrates improvement over previous fits but merely represents the efforts that can and will be undertaken in the future as new, higher resolution observations that highlight regions of the spectrum in which FeH plays an important role are obtained. In this spirit, we plan to incorporate the new FeH opacities derived in this paper into a future, more comprehensive paper that studies the defining FeH and CrH features observed in L dwarf spectra, in particular in the I, Z, J, and H photometric bands.

This work was supported in part by NASA under grants NAG 5-10760 and NAG 5-10629. Support was also provided by the NASA Laboratory Physics Program and the Natural Sciences and Engineering Research Council of Canada. The authors would like to thank Richard Freedman for providing guidance with line-broadening parameters for FeH.

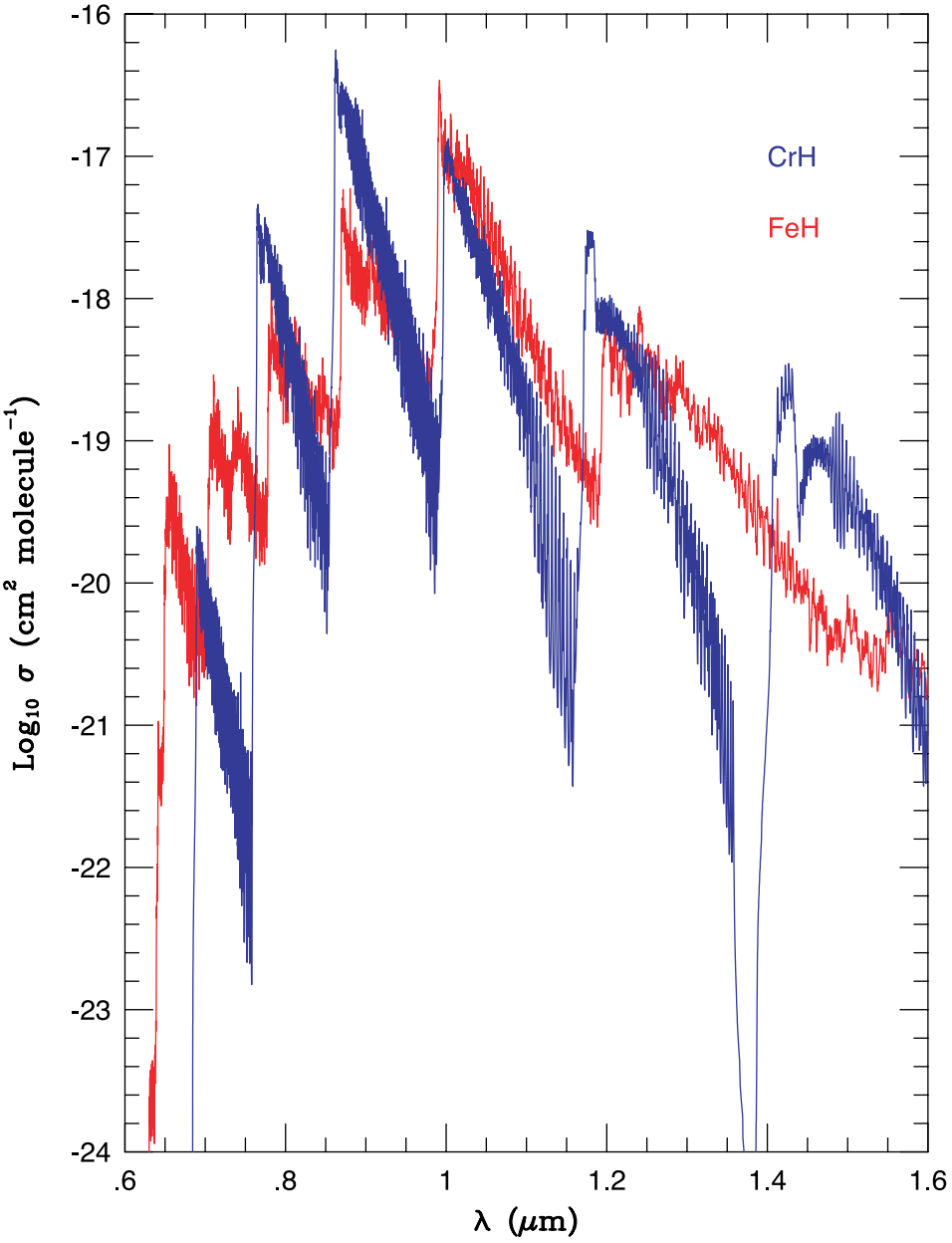

FIG. 1.—Logarithm (base-10) of the absorption cross sections for FeH (*red*) and CrH (*blue*), the former as derived in this paper, the latter taken from Burrows et al. (2002). The temperature and pressure are 1800 K and 30 atm, respectively. Most (but not all) of the important bands for both molecules are to be found at wavelengths between 0.65 and 1.6 μm, and these are what are plotted here. Notice that FeH and CrH frequently contribute opacity in similar wavelength regions. This is particularly relevant around $\sim$0.86 μm, $\sim$1.0 μm, and in the *J* photometric band from $\sim$1.2 to $\sim$1.3 μm.

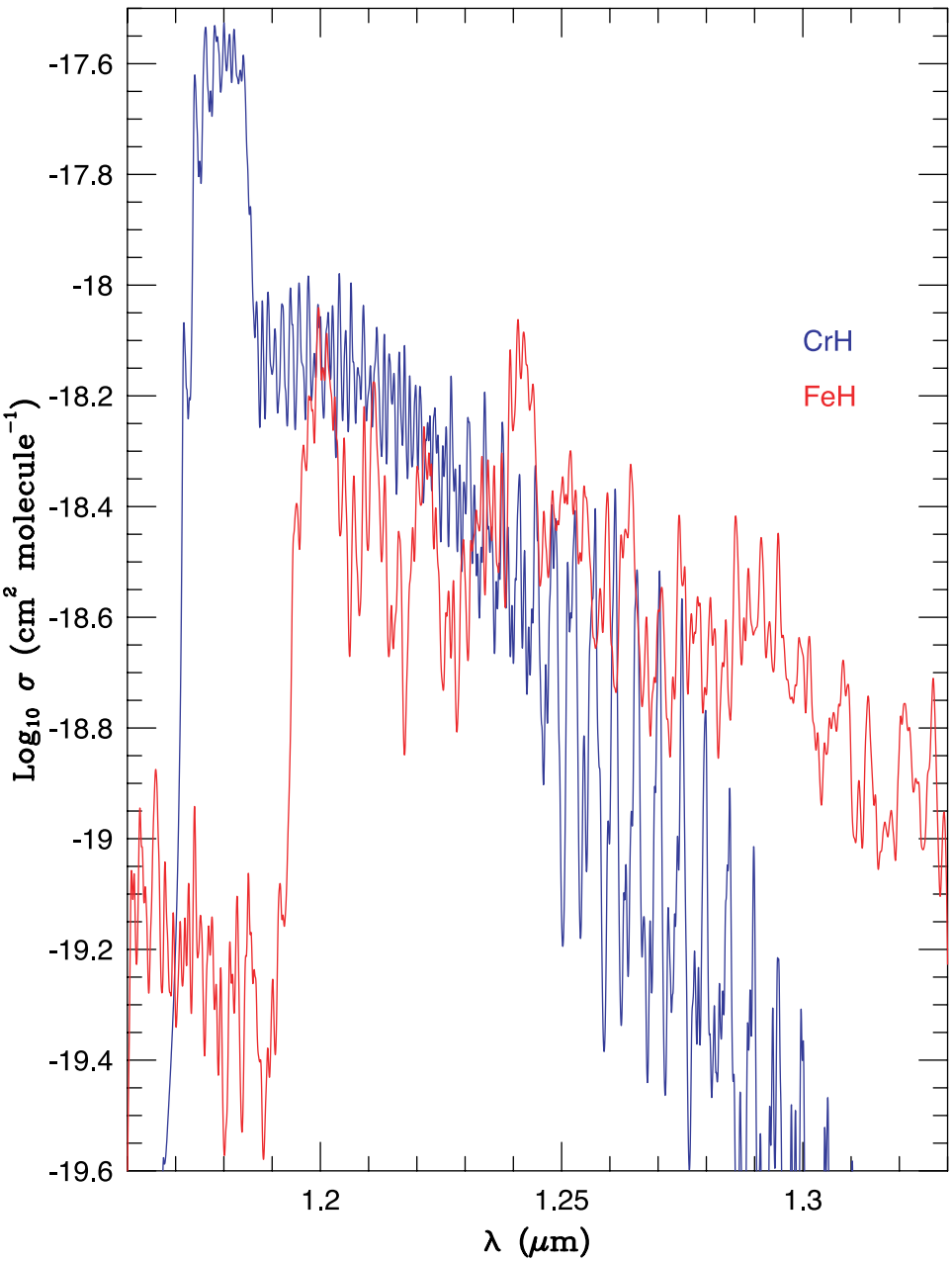

FIG. 2.—Logarithm (base-10) of the absorption cross sections of both FeH (*red*) and CrH (*blue*) in the *J* band from 1.16 to 1.33 μm. As this plot demonstrates, depending on the relative abundances, both FeH and CrH bands can contribute opacity and lines in the *J* band. A spectral resolution near 0.22 cm^{-1} was employed.

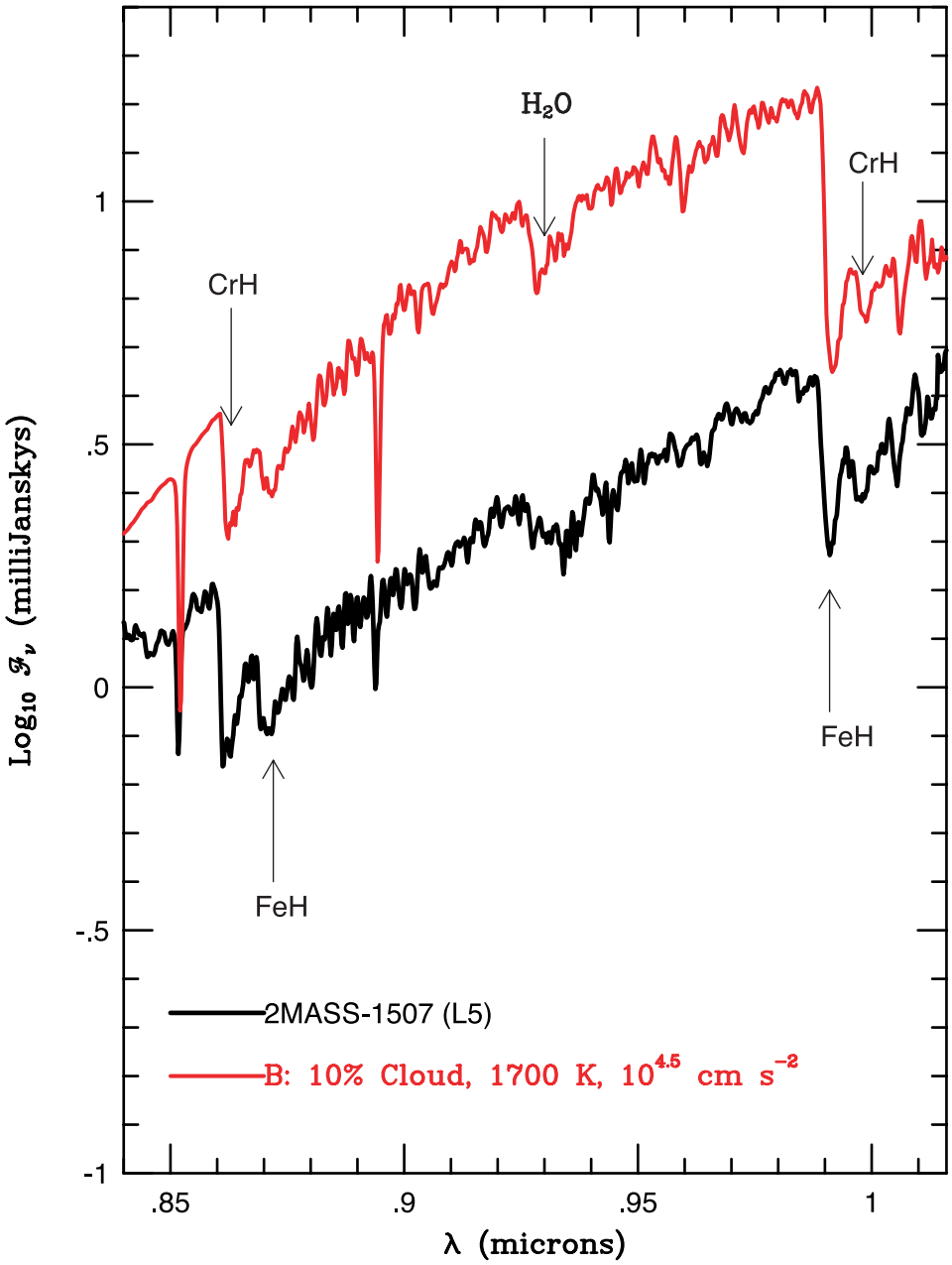

FIG. 3.—Logarithm (base-10) of the absolute flux density ($\mathscr{F}_\nu$) in mJy vs. wavelength (λ) in μm from 0.84 to 1.02 μm for a self-consistent theoretical solar-metallicity model of the L5 dwarf 2MASS-1507. The absolute position of the theoretical spectrum, dependent as it is on the object's unknown radius, was moved up for clearer comparison with the data for 2MASS-1507 (*black*), taken from Kirkpatrick et al. (1999b). The model shown is for $T_{\rm eff} = 1700$ K and a gravity of $10^{4.5}$ cm s^{-2}. The abundance for FeH was calculated using the new thermochemical data derived in this paper and for CrH using the thermochemical data derived in Burrows et al. (2002) and was not adjusted. The new solar abundances from Allende-Prieto et al. (2002) for oxygen and carbon were used, and this has reduced to an acceptable level the depth of the water feature around 0.94 μm. The effects of a forsterite cloud with particles of 50 μm radius incorporating 10% of the available magnesium were included but had only a modest influence in this spectral range. Indicated with arrows are the positions of the CrH, FeH, and H_2O features. Also prominent are the Cs I lines at 8523 and 8946 Å. The resolution of the theoretical spectrum has been reduced so that $R(\lambda/\Delta\lambda)$ is 1000.

REFERENCES

Allende-Prieto, C., Lambert, D. L., & Asplund, M. 2002, ApJ, 573, L137
Balfour, W. J., Lindren, B., & O'Connor, S. 1983, Phys. Scr., 28, 551
Bauschlicher, C. W., Jr. 1995, Theor. Chim. Acta, 92, 183
Bauschlicher, C. W., Jr., Ram, R. S., Bernath, P. F., Parsons, C. G., & Galehouse, D. 2001, J. Chem. Phys., 115, 1312
Bernath, P. F. 1995, Spectra of Atoms and Molecules (Oxford: Oxford Univ. Press)
Brown, J. M., Beaton, S. P., & Evenson, K. M. 1993, ApJ, 414, L125
Brown, J. M., et al. 1975, J. Mol. Spectrosc., 55, 500
Burrows, A., Hubbard, W. B., Lunine, J. I., & Liebert, J. 2001, Rev. Mod. Phys., 73, 719
Burrows, A., Ram, R. S., Bernath, P., Sharp, C. M., & Milsom, J. A. 2002, ApJ, 577, 986
Carroll, P. K., & McCormack, P. 1972, ApJ, 177, L33
Carroll, P. K., McCormack, P., & O'Connor, S. 1976, ApJ, 208, 903
Chertihin, G. V., & Andrews, L. 1995, J. Phys. Chem., 99, 12131
Cushing, M. C., Rayner, J. T., Davis, S. P., & Vacca, W. D. 2003, ApJ, 582, 1066
Dendramis, A., Van Zee, R. J., & Weltner, W., Jr. 1979, ApJ, 231, 632
Dunning, T. H. 1989, J. Chem. Phys., 90, 1007
Fawzy, D. E., Youssef, N. H., & Engvold, O. 1998, A&AS, 129, 435
Hardy, E., & Couture, J. 1988, ApJ, 325, L29

Herzberg, G. 1950, Molecular Spectra and Molecular Structure. I. Spectra of Diatomic Molecules (New York: Van Nostrand)
Hess, B. A. 1986, Phys. Rev. A, 33, 3742
Hullah, D. F., Barrow, R. F., & Brown, J. M. 1999, Mol. Phys., 97, 93
Kassel, L. S. 1933a, J. Chem. Phys., 1, 576
———. 1933b, Phys. Rev., 43, 364
Kendall, R. A., Dunning, T. H., & Harrison, R. J. 1992, J. Chem. Phys., 96, 6796
Kirkpatrick, J. D., Allard, F., Bida, T., Zuckerman, B., Becklin, E. E., Chabrier, G., & Baraffe, I. 1999a, ApJ, 519, 834
Kirkpatrick, J. D., et al. 1999b, ApJ, 519, 802
———. 2000, AJ, 120, 447
Klynning, L., & Lindgren, B. 1973, Univ. Stockholm, Institute of Physics, Rep. 73-20
Knowles, P. J., & Werner, H.-J. 1988, Chem. Phys. Lett., 145, 514
Langhoff, S. R., & Bauschlicher, C. W., Jr. 1990, J. Mol. Spectrosc., 141, 243
Leggett, S. K., Allard, F., Greballe, T. R., Hauschildt, P. H., & Schweitzer, A. 2001, ApJ, 548, 908
McCormack, P., & O'Connor, S. 1976, A&AS, 26, 373
Nordh, H. L., Lindgren, B., & Wing, R. F. 1977, A&A, 56, 1
Partridge, H. 1989, J. Chem. Phys., 90, 1043
Phillips, J. G., & Davis, S. P. 1988, ApJS, 66, 227
Phillips, J. G., Davis, S. P., Lindgren, B., & Balfour, W. J. 1987, ApJS, 65, 721
Schiavon, R. P., Barbuy, B., & Singh, P. D. 1997, ApJ, 484, 499
Schultz, R. H., & Armentrout, P. B. 1991, J. Chem. Phys., 94, 2262
Sharp, C. M., & Huebner, W. F. 1990, ApJS, 72, 417
Stevens, A. E., Feigerle, C. S., & Lineberger, W. C. 1983, J. Chem. Phys., 78, 5420
Tanaka, K., Sekiya, M., & Yoshimine, M. 2001, J. Chem. Phys., 115, 4558
Towle, J. P., Brown, J. M., Lipus, K., Bachem, E., & Urban, W. 1993, Mol. Phys., 79, 835
Walch, S. P. 1984, Chem. Phys. Lett., 105, 54
Wallace, L., & Hinkle, K. 2001a, ApJ, 559, 424
———. 2001b, Sunspot Umbral Spectra in the Region 4000 to 8640 cm^{-1} (1.16 to 2.50 μm), NSO Tech. Rep. 01-001 (Tucson: NSO)
Werner, H.-J., & Knowles, P. J. 1988, J. Chem. Phys., 89, 5803
———. 2002, MOLPRO, Univ. Birmingham
Wilson, C., & Brown, J. M. 1999, J. Mol. Spectrosc., 197, 188
———. 2001, J. Mol. Spectrosc., 209, 192
Wing, R. F. 1972, Mem. Soc. R. Sci. Liège, 3, 123
Wing, R. F., Cohen, J., & Brault, J. W. 1977, ApJ, 216, 659
Wing, R. F., & Ford, W. K. 1969, PASP, 81, 527